Journal of Applied Fluid Mechanics, Vol. 17, No. 9, pp. 2005-2015, 2024.
Available online at www.jafmonline.net, ISSN 1735-3572, EISSN 1735-3645.
https://doi.org/10.47176/jafm.17.9.2546

Flow Characteristics Analysis of Load Rejection Transition Process in Pumped Storage Unit Based on Cavitation Model

Q. Li[1,2†], L. Xin[1], L. Yao[1] and S. Zhang[3]

[1] *School of Energy and Power Engineering, Lanzhou University of Technology 1, Lanzhou, Gansu, 730050, China*
[2] *Key Laboratory of Fluid Machinery and Systems 2, Lanzhou, Gansu, 730050, China*
[3] *Tianjin Key Laboratory of Hydroelectric Power Generating Equipment 3, Tianjin, 300000, China*

†Corresponding Author Email: lqfy@lut.edu.cn

ABSTRACT

Concerning dual-carbon applications, establishing a new energy-dominated power system to achieve carbon peaking and carbon neutrality objectives is imperative. Pumped storage units excel in this context, owing to their unique advantages. During the load-shedding process of the pump turbine, the intricate flow patterns and cavitation phenomena substantially influence the flow field. This study introduces a cavitation model to perform numerical simulations of load rejection processes in pumped storage power plants, aiming to thoroughly investigate the impact of cavitation phenomena on the units. The results indicate that as the rotational speed increases, the dynamic and static interference within the no-blade region becomes notable, resulting in pressure pulsations within the guide vane region and exacerbating structural deformation and fatigue failures. Moreover, deviations from the designated operational point disrupt the symmetry of the flow field, leading to irregular changes in radial forces. Accounting for the mass disturbance and changes in wave velocity attributable to a cavitation phase transition, pressure fluctuation amplitude increases within the draft tube, consequently engendering complex flow phenomena. These findings offer indispensable guidance for the optimal design and safe operation of pump turbines within new power systems.

Article History

Received December 27, 2023
Revised March 23, 2024
Accepted April 5, 2024
Available online July 2, 2024

Keywords:

Pump turbine
Cavitation
Load Rejection Transition Process
Flow Characteristics
Three-Dimensional Numerical Simulation

1. INTRODUCTION

Energy exists in various forms and is broadly categorized into direct and indirect forms. Various energy sources are encompassed within this category, spanning fossil fuels like oil, coal, and natural gas, alongside renewable alternatives such as wind and hydropower. A strong push for hydropower development is essential for climate improvement and advancing the transition of energy structures. Developed countries generally exhibit high hydropower utilization rates, with some exceeding 80%. China possesses abundant hydropower resources; however, its hydropower utilization rate is relatively low, indicating significant development potential. Pumped-storage hydropower stations have several advantages. First, their flexibility enables the effective regulation of peak and off-peak electricity demand, achieving a balance in power demand fluctuations, and reducing dependence on fossil fuels. Second, with the rapid proliferation of clean energy, pumped storage hydropower stations have assumed a critical role in the entire energy system owing to their flexible operational mode and outstanding economic viability. Furthermore, the multiple functionalities of the pumped storage units in the power system, including peak clipping, frequency regulation, phase adjustment, and Crisis Backup , significantly increase the stability and reliability of the power system. In conclusion, pumped-storage hydropower stations represent a mature, clean, efficient, and economically secure means of regulating power systems, contributing significantly to achieving a sustainable and intelligent power supply. Owing to the necessity of meeting the growing load regulation demands of the energy grid, pumped-storage hydropower stations must undergo frequent operational transitions, leading to an increased severity of dynamic instability during unit transition processes.

Compared to traditional hydropower stations, the operation of pumped-storage hydropower stations is more intricate and subject to variability. As per Fig. 1, the pump turbine can operate in five different zones: the pump zone, pump braking zone, turbine zone, turbine braking zone, and reverse pump zone (Li, 2012). The large impeller

NOMENCLATURE

ρ	fluid density	σ_k	Prandtl number corresponding to turbulent kinetic energy
k	turbulent kinetic energy	G_k	turbulent kinetic energy due to average velocity gradient
t	time	σ_ε	prandtl number corresponding to turbulent dissipation rate
u	X-direction velocity	ε	turbulent dissipation rate
v	Y-direction velocity	C_1	a coefficient related to viscosity
w	Z-direction velocity	E	shear strain rate
μ	fluid viscosity	a_0	guide vane opening
μ_t	turbulent viscosity		

diameter of the pump turbine results in a significant centrifugal force. The water flow velocity in the turbine direction decreased sharply, causing the opening line to rapidly bend downward at a small angle from the runaway line (M_{11}=0). This allows the unit to potentially enter the braking zone after runaway, forming an "S" shape. In the "S" characteristic zone, the same unit speed (n_{11}) may correspond to multiple different unit flow rates (Q_{11}), including flow rates entering the reverse pump zone. During operation in the "S" characteristic zone, the pump turbine is susceptible to transitioning directly from runaway conditions to reverse pump conditions. In this situation, the impeller rotates in the same direction as in turbine conditions, but the torque it experiences is opposite to the rotation direction, which may cause the unit structure to impact loads, leading to potential damage to the overflow components. Additionally, the interplay between the blade and the water flow induces pronounced pressure oscillations of high intensity, potentially making it challenging for the unit to synchronize with the grid (Yue et al., 2018). In the operational phase of the pump-turbine, the rejection of load emerges as the most critical transient procedure, constituting an inevitable transitional phase (Fu & Li, 2018). Scholars have undertaken substantial research efforts, both domestically and internationally, regarding the transition processes of pumped-storage hydropower stations. Pejovic et al. (1976) first discovered and studied the "S" characteristic zone in the 1970s. Chen & Xie (2001) conducted model experiments to test the pressure pulsations inside an impeller passage. Simultaneously, they obtained the flow properties of the internal water flow in the impeller passage through visualization experiments, revealing the flow condition changes in the "S" characteristic zone and analyzing the reasons for the unstable flow state in the "S" characteristic zone. Hasmatuchi et al. (2011) conducted visualization experiments on a pump turbine and concluded that the flow in the guide vane passage was stable within the normal operating range. However, under no-load conditions, rotational instability leads to a chaotic flow inside the passage. This phenomenon became more severe when the flow rate approached zero, with a noticeable backflow between the double-row guide vanes. Kubota & Kushimoto (1978) conducted experimental research on high-head pump turbines, performed visualization

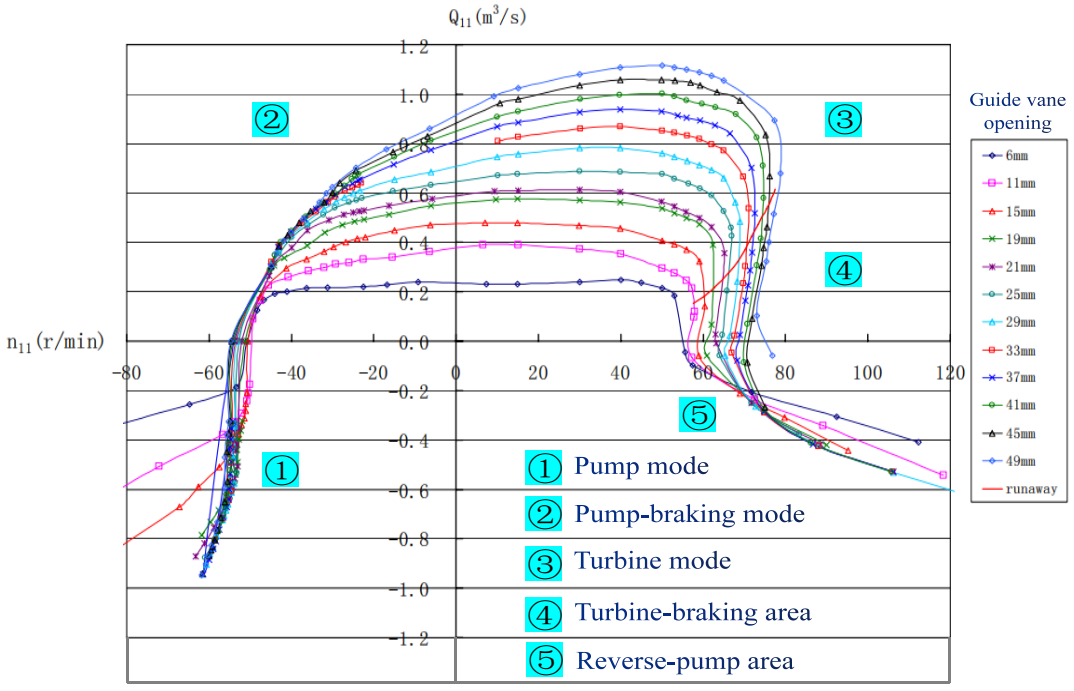

Fig. 1 Overall Characteristic Curve of Pump-Turbine

experiments to observe the inner flow characteristics of the unit, and conducted in-depth studies on variations in reverse pump conditions. The maturation of three-dimensional Computational Fluid Dynamics (CFD) for numerical simulations of hydraulic machinery has been expedited by the swift progression of computer technology. The "S" characteristic of pump turbines is a significant cause of their operational instability. Pump turbines typically pass through the "S" characteristic zone during transient operation. To address the instability issue in the "S" characteristic zone, one engineering approach is to use different guide vanes to guide the unit away from the "S" characteristic zone during operation (Xiao & Xiao 2014). Li et al. (2021, 2013 2020) conducted research analyzing the influence mechanism of asynchronous guide vanes on the internal flow characteristics in the "S" characteristic zone of pump turbines. Peng et al. (2021) studied and analyzed the impact of impeller characteristics on the transition process of pumped-storage hydropower stations. Pumped storage plants often undergo transient processes due to the intermittent and unpredictable nature of renewable energy sources. During load rejection processes in PSPs, significant fluctuations in rotating speed and pressure may lead to serious accidents (Mao et al., 2021). Goyal et al. (2021) employed a cavitation model to numerically simulate and analyze the load-rejection transition process of a pump turbine. They discovered that cavitation during load rejection mainly occurred on the backside of the close-by blades the top cover and summarized the vortex evolution process in the tailrace. Zuo et al. (2015) discovered that the turbine's performance curve in turbine mode exhibits an S-shaped feature, resulting in instability issues during the transient process. These challenges encompass difficulties in synchronization during grid start-up and instability during load rejection. Luo (2022) delved into the impact of the "S" characteristic on the load rejection transition process. He summarized an optimal guide vane closure pattern based on the transitional coefficient of the "S" characteristic and analyzed the correlation between the "S" characteristic and water hammer pressure. Wan (2023) optimized the guide vane control strategy to address the issue of large fluctuations during the transition process. Additionally, they utilized a model to predict the transition process, establishing a foundation for the secure and steady functioning of a power station. During the operation of the unit, it undergoes a transition process between the pump and turbine operating conditions, which is a critical factor in determining the stability of the power station. In actual operation, the unit transition process includes three repetitive stages: turbine, braking, and pump backflow. The instability phenomenon in the "S" characteristic zone during the transition process significantly affects system extremes such as pressure and speed, posing a serious threat to power generation and grid connection (Xu, 2022).

This investigation delved into the flow cavitation features exhibited by a pump turbine in the context of load rejection, employing three-dimensional computational fluid dynamics technology. The complex flow mechanism during load shedding was revealed by analyzing the flow characteristics under various working conditions. This research makes significant theoretical contributions to the study of transient dynamics in pump turbines, which are of great significance for enhancing the safety of pump turbine transient processes and hydraulic system stability. Moreover, this research provides reliable physical and mathematical models for the optimization design and operation prediction of pump turbine structures. This establishes a robust groundwork for the prospective evolution of digital twin systems applied in pumped-storage power plants.

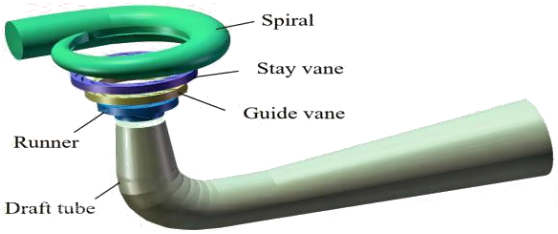

Fig. 2 Calculation area of the water pump turbine model

Table 1 Pump-turbine's geometric parameters

Parameter	Symbol	Value
Runner's high-pressure side diameter /mm	D_1	473.6
Runner's low-pressure side diameter /mm	D_2	300
Blade count of the runner	Z_r	9
Number of guide vanes	Z_g	20
Number of stay vanes	Z_s	20
Tailrace outlet diameter /mm	D_{1m}	660
Volute inlet diameter /mm	D_{2m}	315
Height of guide vanes /mm	b_0	66.72
Case wrap angle/(°)	φ_0	343

2. NUMERICAL MODELING AND COMPUTATIONAL TECHNIQUES

2.1 Numerical Domain and Mesh Creation

The model for the numerical simulation in this study comprises five components: volute casing, fixed guide vane, movable guide vane, impeller, and tailrace, as depicted in Fig. 2. Table 1 contains a catalog of the principal parameters.

The numerical simulation area of the pump turbine was meshed using ICEM (Ansys), employing a single-structure "O"-type mesh division for the guide vane region. Considering the practical computational resources, a hexahedral mesh model was utilized to ensure the accurate calculation of small flow channel areas and improve the calculation accuracy. The boundary layers of the blade, volute casing, and guide vane were refined to enhance the precision of the wall surface simulation. Figure 3 shows a schematic of the overall mesh division of the pump turbine.

2.2 Grid Independency Verification

To avoid the significant influences of changes in other conditions on the calculation results, grid independence verification was performed before the calculation. The

Table 2 Grid segmentation for individual parts

Parameter	Spial Casing & Stay vane	Guide vane	Runner	tailrace
Total elements	1895767	1319500	1505507	1656365
Total nodes	406840	1128400	1227820	1592144
Min angle /(°)	18	29	30	36
Min quality	0.51	0.48	0.52	0.66

Table 3 Comparative assessment of simulation outcomes and test results

Condition	Turbulence model	Q_{s11}	n_{s11}	Q_{t11}	n_{t11}	ΔQ_{11}	Δn_{11}
OP.1	Realizable *k-ε*	0.150	57.61	0.152	57.623	1.32	0.02
	Standard *k-ω*	0.147	55.20.	0.152	57.623	3.29	4.20
	SST *k-ω*	0.149	56.90	0.152	57.623	1.97	2.99
OP.2	Realizable *k-ε*	0.271	65.3	0.276	66.217	1.81	1.38
	Standard *k-ω*	0.274	64.08	0.276	66.217	0.72	3.23
	SST *k-ω*	0.266	64.30	0.276	66.217	3.62	2.90

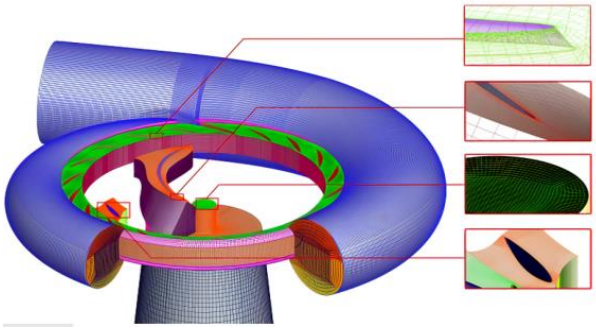

Fig. 3 Schematic of Local Grid

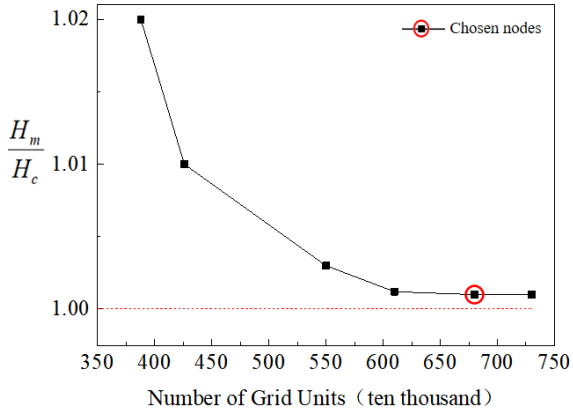

Fig. 4 Grid Independence Verification

error was defined as $H_m \cdot H_c^{-1}$, where H_c is the calculated head and H_m is the experimental head. As shown in Fig. 4, the error decreases with an increase in the number of grids. However, when the error curve tends to be horizontal after reaching a certain point, the error almost no longer changes when the grid count surpasses 6.75 million. At this point, the error was < 3.2%. Therefore, considering both the calculation accuracy and economy, the final decision was to set the number of grids to 6.8 million. The grid division results are listed in Table 2. The selected grid scale satisfies the requirements of wall Y+ in the turbulent flow calculations, as shown in Fig. 5, which illustrates the Y+ distribution on the moving blade surface.

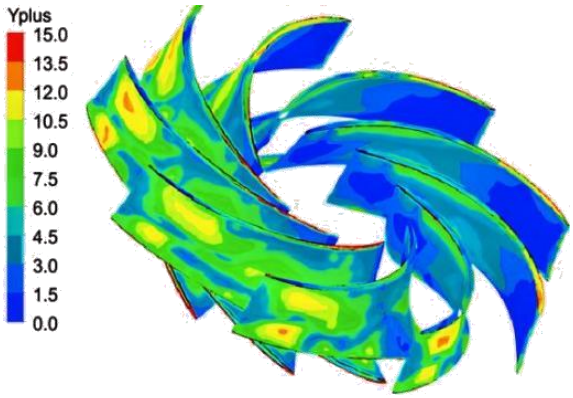

Fig. 5 Y+ Distribution on the Surface of Impeller Blades

2.3 Governing Equation and Boundary Conditions

For the stable simulations of incompressible flows in this investigation, the application of ANSYS FLUENT 15.0 was executed. The finite volume method was employed to solve the Reynolds-averaged Navier-Stokes equations. To compare the performance of different turbulence models, three models: Realizable *k-ε* model, Standard *k-ω* model, and the SST (transport of shear stress) *k-ω* model were selected. Simulations were conducted at operating points OP.1 and OP.2, and the relevant computational results are listed in Table 3. Comparison of simulation and experimental results for different turbulence models reveals the following: in OP.1, the Realizable *k-ε* turbulence model has the smallest errors for both unit rotational speed and unit flow rate; in OP.2, the Realizable *k-ε* turbulence model has the smallest error for unit rotational speed, while the Standard *k-ω* turbulence model has the smallest error for unit flow rate, but the error for unit rotational speed is much higher compared to other models. Furthermore, considering the superior performance of the Realizable *k-ε* turbulence model in simulating wall vortices during load dumping processes, as well as its excellent performance in simulating shear flows (jets, mixed flows, and separated flows) (Li et al., 2023), it is concluded that the Realizable *k-ε* turbulence model is more suitable for simulating

Table 4 Boundary criteria

Boundary Condition Classification	Boundary Condition Setup
Inlet	Mass Flowrate
Outlet	Outflow
Interface	Mesh Interface
Wall-Adjacent Treatment	Standard Wall Function and No-Slip Constraint
Conditions in the Runner's Cell Zone	Steady Movement in Multiple Reference Frames Mesh Motion in Transient Conditions

transitional processes.

(Q_{s11} represents the simulated flow rate with a unit of m^3/s, and n_{s11} represents the simulated speed in r/min. Similarly, Q_{t11} is used for the experimental test flow rate with a unit of m^3/s, and n_{t11} denotes the experimental test speed in r/min)

The flow control equation set for the Realizable *k*-*ε* model is selected as follows:

Reynolds equation:

$$\frac{\partial(\rho u_i)}{\partial t}+\frac{\partial(\rho\overline{u_i u_j})}{\partial x_j}=-\frac{\partial p}{\partial x_i}+\frac{\partial}{\partial x_j}(\mu\frac{\partial u_i}{\partial x_j}-\rho\overline{u_i' u_j'})+S_i \tag{1}$$

Continuity equation:

$$\frac{\partial\rho}{\partial t}+\frac{\partial(\rho u)}{\partial x}+\frac{\partial(\rho v)}{\partial y}+\frac{\partial(\rho w)}{\partial z}=0 \tag{2}$$

k-equation

$$\frac{\partial(\rho k)}{\partial t}+\frac{\partial(\rho k u_i)}{\partial x_i}=\frac{\partial}{\partial x_j}[(\mu+\frac{\mu_t}{\sigma_k})\frac{\partial k}{\partial x_j}]+G_k-\rho\varepsilon \tag{3}$$

ε-equation:

$$\frac{\partial(\rho\varepsilon)}{\partial t}+\frac{\partial(\rho\varepsilon u_i)}{\partial x_i}=\frac{\partial}{\partial x_j}[(\mu+\frac{\mu_t}{\sigma_\varepsilon})\frac{\partial\varepsilon}{\partial x_j}]+\rho C_1 E\varepsilon-\rho C_2\frac{\varepsilon^2}{k+\sqrt{v\varepsilon}} \tag{4}$$

The Fluent software platform incorporates two built-in cavitation models: Schnerr–Sauer and Zwart–Gerber–Belamri models. The Zwart–Gerber-Belamri model, derived from the simplified Rayleigh–Plesset equation, offers superior predictive capabilities for unsteady cavitation flow analysis compared with the Schnerr–Sauer model. Additionally, it exhibited excellent convergence properties, making it well suited for the investigation of load-shedding phenomena in this study. Consequently, the Zwart model was selected as the preferred approach for cavitation flow calculations.

The governing equation of the Zwart cavitation model is shown in Equation 5:

$$m=\begin{cases}F_e\dfrac{3\alpha_{nuc}(1-\alpha_v)\rho_v}{R_s}\sqrt{\dfrac{2}{3}\dfrac{p_v-p}{\rho_1}} & (p\le p_v)\\ F_c\dfrac{3\alpha_v\rho_v}{R_B}\sqrt{\dfrac{2}{3}\dfrac{p-p_v}{\rho_1}} & (p>p_v)\end{cases} \tag{5}$$

In the equation: the variable "m" denotes the rate of mass transfer occurring between the liquid and vapor phases; α_{nuc} epresents the initial gas phase volume fraction at the nucleation site, set at $5.0\cdot10^{-4}$; α_v represents the volume fraction of cavitation; R_B represents the cavitation bubble radius, set at $1.0\cdot10^{-6}$; F_e represents the empirical coefficient for the evaporation process, set at 50; F_c represents the empirical coefficient for the condensation process, set at 0.01; P_v represents the saturation vapor pressure; ρ_v represents the bubble density; ρ_l represents the fluid density.

During the grid-connected power generation process of a water pump hydroturbine, if the generator suddenly disconnects from the power grid because of electrical or mechanical failures, a load-rejection process will occur. In order to ensure safety, it is necessary to brake the unit by closing the guide vanes. Therefore, to reproduce this process in a numerical simulation, a dynamic mesh technology is required. The use of a fluent dynamic mesh requires the solver to adjust the distribution of mesh nodes automatically based on the movement and deformation of the boundaries. The expression of the conservation equation for a general scalar within an arbitrary control volume V, incorporating boundary movement, is presented as follows:

$$\frac{\mathrm{d}}{\mathrm{d}t}\int_V\rho\phi\mathrm{d}V+\int_{\partial V}\rho\phi(\boldsymbol{u}-\boldsymbol{u}_\mathrm{g})\mathrm{d}\boldsymbol{A}=\int_{\partial V}\Gamma\nabla\phi\mathrm{d}A+\int_V S_\phi\mathrm{d}V \tag{6}$$

V(t) denotes the changing control volume, while ∂V(t) represents its moving boundary. Additionally, $\boldsymbol{u}_\mathrm{g}$ is the velocity of the moving grid; ρ stands for fluid density; $\bar{u}$ is the fluid velocity vector; Γ represents the dissipation coefficient, and S_ϕ is the source term in the scalar field.

Boundary conditions are detailed in Table 4.

To capture the evolution process of the vortices accurately, this study used a sufficiently small numerical calculation time step and implemented the coupling of the velocity and pressure using the SIMPLEC algorithm. The pressure term was discretized using a second-order upwind scheme, with the accuracy set to $1\cdot10^{-6}$. In the unsteady-state calculation, the time step was set to the time required for the impeller to rotate by 3 °, and 20 iterations were performed for each time step, totaling 2400 time steps, equivalent to simulating 20 impeller rotations, to obtain more accurate results. Convergence was considered achieved when the static pressure values at the inlet and outlet exhibited regular changes, and the numerical simulation results were output.

The head value for the simulation experiment was set as H=30m. The inlet of the tailrace pipe adopted a total pressure inlet, and the outlet of the spiral case was subjected to a specified static pressure. A sliding mesh was used to handle the dynamic–static interference, and an interface was set at the junction. First, the Realizable *k*-*ε*

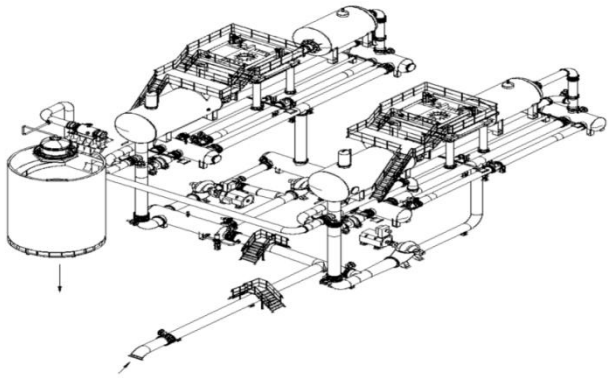

(a) Layout Diagram of Hydraulic Machinery Model Universal Test Bed

(b) Panoramic View of Pump turbine Test Bed

(c) Pump turbine Test Bench

Fig. 6 Experimental Diagrams for Pump turbine

turbulence model was used for single-phase flow simulation of clear water, and then the results of steady-state calculations were used as initial conditions for unsteady-state calculations. The saturation vapor pressure was established at 3540 Pa, with the liquid phase's volume fraction set to 1 at the inlet, while the vapor phase's volume fraction was specified as 0. In the solving process, the utilization encompassed the application of the SIMPLEC algorithm along with a second-order upwind scheme and the time step for unsteady-state calculations was set to $\Delta t=4.673\cdot10^{-4}$s, with a residual of 10^{-6} as the convergence criterion for iterative calculations.

2.4 Experimental validation

The experiments were conducted on the Testbed at the laboratory designated as the Key Laboratory of Hydraulic Machinery Equipment in Tianjin, China. The experimental head was determined by measuring the pressure difference using the numerical value of 30m. The experimental setup for the pump turbine is displayed in Fig. 6; the operation strictly followed the IEC60193 standard and other experimental specifications. Table 5 presents the test parameters used in the experiments. These experiments aimed to make full use of the experimental platform to secure correctness and reliability of the experimental results.

Table 5 Experimental Platform Parameters

Type of drive pump	34S4-19×1
Maximum head/ m	30
Mass flow maximum / (m^3/s)	2.0
Runner diameter / (mm)	380
Dyno power / (kW)	540
Dyno Rotation Speed / (r/min)	0～2600
Pump Motor Power/ (kW)	593
Drive Pump speed/ (r/min)	0～1200
Flow calibration container volume/ (m^3)	120×2
Reservoir volume / (m^3)	750

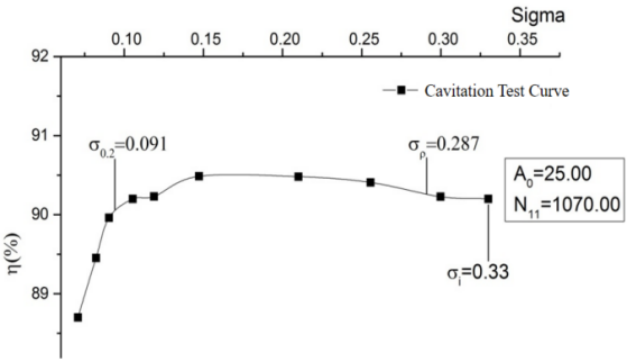

Fig. 7 Preliminary Acceptance Test Results of Cavitation in Pump Operation Zone for Model

The experiment was conducted in accordance with GB/T3216-2005 standards. The flow rate was maintained constant during the experiment and cavitation was induced by lowering the inlet pressure of the tailwater pipe to increase its inlet vacuum of the tailwater pipe. As the inlet pressure continued to decrease, the degree of cavitation inside the unit gradually increased, particularly on the blades, leading to a sharp decrease in pump efficiency. To facilitate the processing of experimental data and numerical calculations, the cavitation number σ was introduced.

$$\sigma = \frac{P_{in} - P_v}{0.5\rho u_2^2} \tag{7}$$

In the formula, P_{in} denotes the impeller's inlet pressure, Pa; P_v represents the saturation vapor pressure, Pa; ρ stands for the density of the working medium, kg/m³; and u_2 represents the circumferential velocity at the impeller outlet, measured in m/s.

A pump turbine with a guide vane opening of a_0=33 mm was selected as the research object. The inlet vacuum of the tailwater pipe was changed by changing the inlet pressure of the tailwater pipe to obtain the corresponding experimental data, as shown in Fig. 7. By comparison with the numerical calculations, it was found that their changing trends were basically consistent, and the error was within an acceptable range. This affirms the dependability of the numerical computation in forecasting the cavitation performance of the pump turbine across varying cavitation numbers. The characteristic curves for different cavitation numbers are shown in Fig. 8.

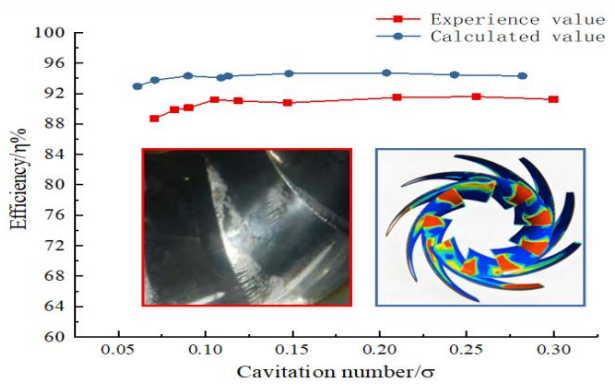

Fig. 8 Performance curves depicting cavitation at different cavitation numbers

3. FINDINGS AND ANALYSIS

3.1 Analysis of Pressure Pulsations in the Unbladed Region during Load Rejection

To better describe the variation of pressure pulsation amplitude intensity in the unbladed region of the pump turbine, a dimensionless quantity, the relative pressure pulsation amplitude $\Delta H/H$, is introduced as a reference value to quantify the intensity of pressure pulsation in the pump turbine. Four monitoring points were arranged uniformly on the midstream surface, depicted in Fig. 9.

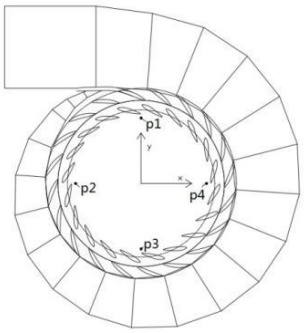

Fig. 9 Pressure pulsation monitoring locations in the unbladed region

Processing of the pressure pulsation signals obtained from the detection points involves introducing a dimensionless parameter $\Delta H/H$ to represent the fluctuation of static pressure at each monitoring point. In the study, the abscissa is the ratio of the monitoring frequency to the rotational frequency, i.e., the horizontal axis is f/f_n, and the vertical axis is the peak amplitude of the frequency signal $\Delta H/H$. The introduced dimensionless parameter formula $\Delta H/H$ is used to measure the magnitude of static pressure fluctuations, as shown in Formula 8:

$$\Delta H / H = \frac{P_i - \overline{P}}{\overline{P}} \tag{8}$$

In the formula: $\Delta H/H$ is the relative amplitude (%), P_i is the pressure detection value (Pa), and $\overline{P}$ is the average pressure at the monitoring point (Pa).

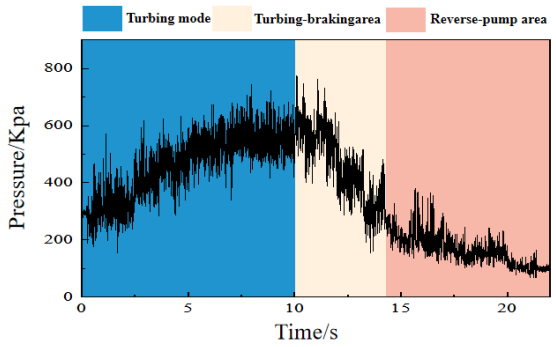

(a) Time-domain depiction of pressure fluctuations at point p1.

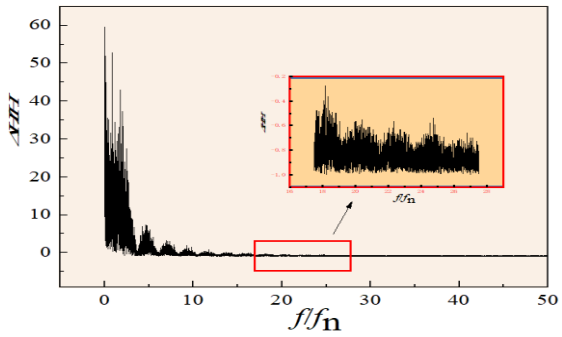

(b) Frequency domain plot of pressure pulsations at point p1.

Fig. 10 Time and frequency-domain charts depicting pressure pulsations at point P1

Figure 10 depicts the pressure pulsations at point P1 during the load rejection process of the pump turbine, both in the time and frequency domains. The flow characteristics of the unit primarily stem from the pressure fluctuations and dynamic instability. Throughout the load rejection process of the pump turbine, the unit underwent turbine operating, braking, and reverse pumping conditions. The flow changes within the runner area were extremely intense. In Fig. 10(a), from 0 to 10 s, the unit is in the turbine operating condition, with the adjustable guide vanes almost unchanged, a large flow, and the impeller gradually increasing to the runaway speed. This leads to a numerical increase in the pressure pulsations in the impeller owing to the centrifugal force and inflow of the guide vanes. From 10 s to 14 s, the unit entered the braking condition, with the flow gradually decreasing to zero and the speed slightly decreasing. Influenced by the inertia of the large flow fluctuations in the previous stage, the pressure pulsation values in the runner area increased slightly before quickly decreasing, and the impeller torque reversed to a negative value. The load rejection process continued from 14 s to 20 s, and the unit was in the reverse pumping condition. Influenced by the "S" characteristic, the speed fluctuation decreases and then increases rapidly, while the flow first decreases before fluctuating upward. In a short time, the unit generates a tremendous torque reversal on the main shaft, which can potentially cause structural deformation and fatigue damage. To analyze the frequency-domain characteristics of pressure pulsations during the load rejection process, the transformation of time-domain pressure pulsation values was accomplished

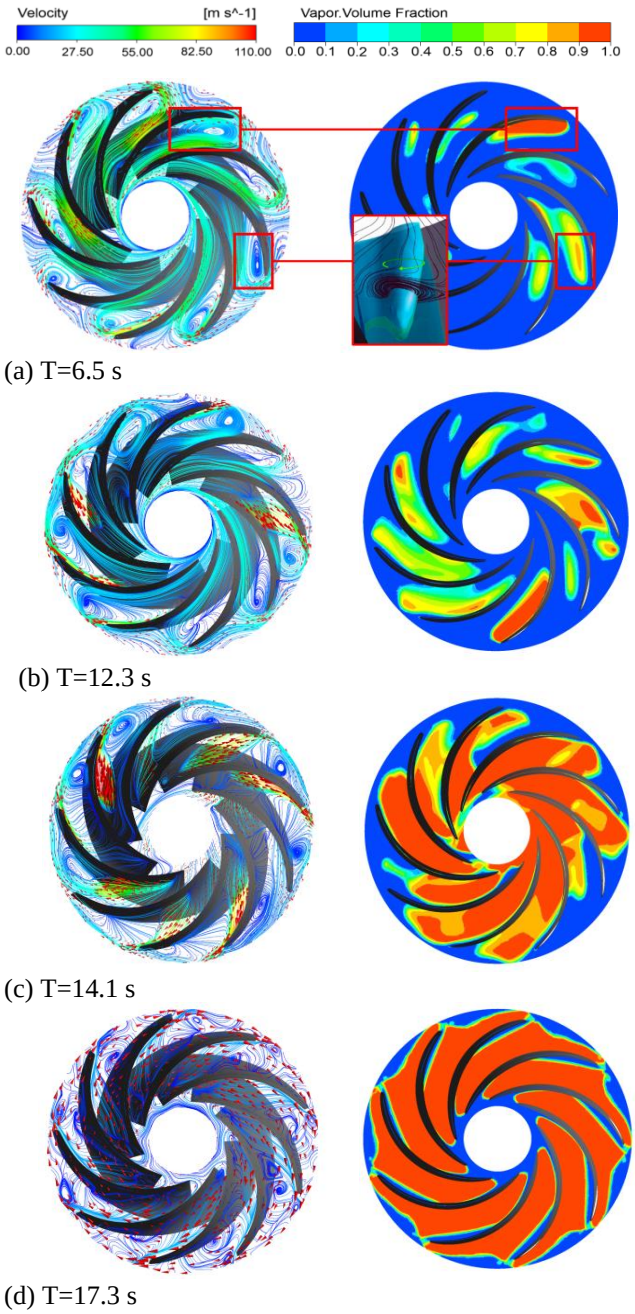

(a) T=6.5 s

(b) T=12.3 s

(c) T=14.1 s

(d) T=17.3 s

Fig. 11 Distribution map of streamlines and void volumes in the impeller region during load rejection

using the short-time Fourier transform. Figure 10(b) shows the spectrum of pressure pulsations at point P1. The rotational speed varies in response to changing working conditions, causing corresponding fluctuations in blade frequency and resulting in a noticeable peak in amplitude at the blades' traversal frequency. High-frequency pressure pulsations in the curve display discernible periodicity and a general tendency towards decreasing amplitude. An increase in f/f_n is observed to stabilize the frequency of pressure pulsations. In the range of $17.5f_n$ to $27.5f_n$, the concentrated region widens. This phenomenon occurs during load rejection, leading to the closure of movable guide vanes and the combined impact of rotational speed and flow, causing a more pronounced disturbance in the flow state within the bladeless region. The bladeless water ring sustains varying degrees of damage, intensifying flow disorder, complicating vortex motion, and expanding the range of pulsation manifestation, all resulting from the interaction of movable guide vanes closure, rotational speed, and flow during load rejection. The intricate movement of vortices within the passage emerges as the primary factor influencing low-frequency pulsations.

3.2 Analysis of Streamlines and Void Volume Distribution

As shown in Fig. 11. To better explain the reasons for the pressure pulsation changes in the bladeless area during the load rejection process mentioned earlier, streamlines and void volume distribution maps at different time periods of this process (a for the turbine mode, b for the braking mode, c for the eve of the reverse pump mode, and d for the reverse pump mode) were selected for analysis. To be concise, the word "relative" is omitted in the following text. At time T=6.5 s, the operating condition of the unit is near the "S" characteristic, deviating from the design operating point, resulting in a large incidence angle, which is prone to flow separation and vortices, but the influence range of these effects is relatively small. The interference between the dynamic and static effects and the off-flow effects of the impinging blades are intertwined, leading to the formation of a low-pressure area at the center of the vortex in the blade passage area, preliminarily forming a wing-attached cavitation. With an increase in the upstream flow and speed, an unstable flow in the passage is induced, causing intense hydraulic vibration. In this process, with pressure changes in the natural flow, the formation and collapse of cavities occur repeatedly. Under braking conditions (T=12.3 s), with a rapid decrease in the flow rate, the pressure pulsation quickly decreased after a short period of inertial impact. Large-scale vortices emerge in the blade inlet area with a wide range of influences and long durations. Simultaneously, the cavity expands and undergoes displacement, increasing the intensity of the vortices squeezing in the blade passage and leading to a sharp drop in the local pressure in this area. Under the reverse pump condition (T=14.1 s), an obvious semi-cavitating flow appeared in the runner, and severe flow separation and backflow occurred in the passage, resulting in a chaotic flow. The interaction between the vortices was enhanced, and the influence of the vortices on the cavitation flow was significant. The entire blade passage was filled with vortices and the flow became unstable, whereas the cavities tended to spread towards the outlet area.

3.3 Analysis of Radial Force of Runner During Load Rejection

Force is the direct cause of material damage and vibration, and there is a close relationship between the vibration of the impeller and the material damage caused by force (Qian et al. 2008, 2018). When conducting an unsteady force analysis, it is essential to consider two force characteristics during the design or selection of pump turbines: axial and radial. When a pump turbine operates as a pump, the vortex and backflow around the tongue in the volute casing result in significant hydraulic asymmetry around the impeller. This affects the propagation of dynamic and static interference, leading to

a more uneven pressure distribution compared with the turbine operation, thus causing asymmetric radial water thrust. Owing to the difference in water pressure between the high- and low-pressure sides of the outer circumference of the impeller, an axial force is formed. When monitoring the overall radial forces in the X- and Y-directions of the impeller during multiple numerical calculations, there may be some differences in the radial force values monitored multiple times under the same operating conditions. To reduce the impact of this difference on the accuracy of the results, this study adopted an averaging method. In the numerical calculations, a total of 20 iterations were executed for each time step, and the average of these 20 iterations was considered the radial force value for that time step, as expressed in Equation 9 and 10.

$$F_R = \sqrt{F_x^2 + F_y^2} \tag{9}$$

$$F_{RMS} = \sqrt{\frac{1}{20}\sum_{i}^{20} F_{Ri}^2} \tag{10}$$

International standards impose strict limits on the main shaft vibration displacement of pump turbine units because it is directly related to the safety of the unit operation (Zhang et al., 2019). Figure 12 shows the variation in the combined radial force of the impeller during the load rejection process. During one revolution of the impeller, the combined radial force under transient conditions exhibited continuous cyclic variation. During the monitoring period, owing to the cavitation development, the difference in the instantaneous radial force between the initial and final moments gradually increased. In the initial stage, the eccentricity of the radial force is caused by the unbalanced force on the impeller owing to the blockage in the passage. At this time, the flow pattern in the impeller region exhibits a double-stall vortex, leading to the generation of a nonsymmetric radial force on the impeller and significant fluctuations in the radial force. This may cause eccentricity of the turbine unit rotor, induce shaft whirl, exacerbate shaft system wear, and even lead to serious accidents, such as rotor-stator collisions. Examination of transient processes has revealed the deleterious impact imparted by features adopting an S-shaped configuration. Changes in the axial force are mainly influenced by complex internal flows, particularly during load–rejection transition processes. With changes in the flow rate, longitudinal transition instability occurs continuously in the inlet flow pattern of the impeller, and the dynamic-static interference in the bladeless zone adds to the impact on the pressure field. Blade vortices are generated in the impeller flow passage, and in severe cases, they may block the passage, leading to a rotational stall. Near the impeller discharge cone, the derivation and breakup of tailwater vortices occurred continuously. These changes in the internal flow significantly affect the radial force pulsation signal, causing the radial force trajectory to no longer close, which is another phenomenon caused by the cavitation process.

Within the flow exhibiting cavitation, owing to the expulsion effect of the cavities, the effective cross-sectional area for the water passage decreases, and the flow velocity in the unblocked blade passages significantly increases, affecting the impeller inlet angle. The mutual influence between adjacent blade passages is continuously transmitted, leading to non-closure of the radial trajectory over one revolution. In addition, the repeated and random occurrence of cavity birth, expansion, compression, and collapse processes disrupts the symmetry of the flow field variations under single-phase flow conditions, thereby disrupting the periodicity of the radial force changes. Simultaneously, the symmetry of the radial force was severely disrupted, and the radial swing amplitude of the unit increased. These discoveries underscore the intricacy of flow characteristics in pump turbines operating under multifaceted conditions, influenced by a multitude of factors.

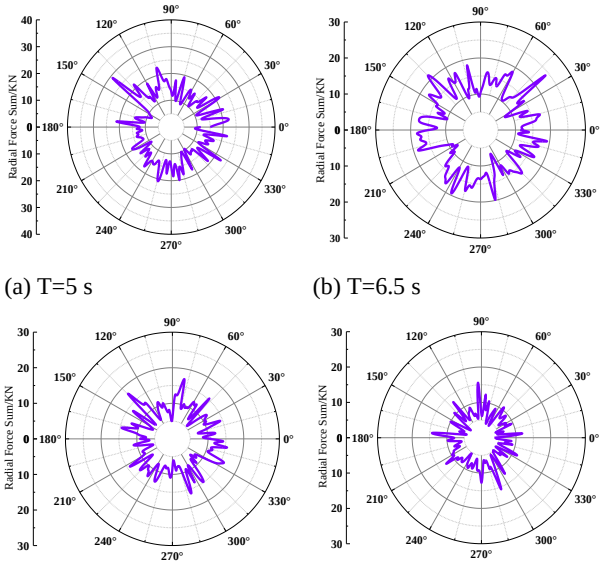

(a) T=5 s (b) T=6.5 s

(c) T=12.3 s (d) T=14.1 s

Fig. 12 Radial Force Combination of Impeller during Load rejection Process

3.4 Evolution of Internal Flow in the Tailrace under Load Rejection

Figure 13 presents the distribution of streamlines within the tailrace throughout the load-rejection process. In the initial stage of load rejection (T=5s), the flow velocity was mainly distributed in the middle and partial walls of the tailrace, with good flow conditions and no obvious cavitation. As the speed increases (T=6.5s), a helical cavitation vortex appears in the tailrace, and the vortex rotates in correspondence with the impeller's direction of rotation. The appearance of the helical cavitation vortex increases the pressure pulsation amplitude on the tailrace wall. Significant unit vibration problems may occur when the characteristic frequency of an unstable cavitation vortex is close to the natural frequency of the unit. In the early stage of entering the reverse pump condition (T=14.1s), the flow direction changed and a large amount of backflow occurred in the straight cone section of the pipe. At this time, the vortex structure was squeezed towards the tailrace wall, leading to a sharp increase in the flow velocity on the wall. When the unit is deeply immersed in the reverse pump condition

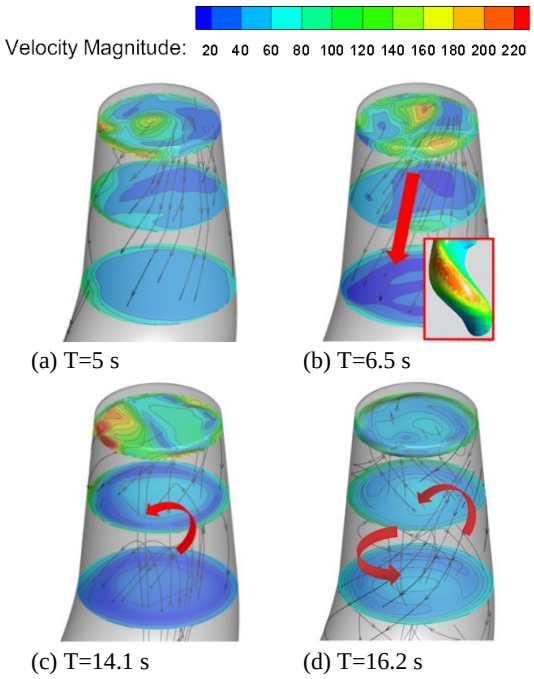

(a) T=5 s (b) T=6.5 s

(c) T=14.1 s (d) T=16.2 s

Fig. 13 Evolution of internal flow in the tailrace during the load rejection process

(T=16.2s), the flow in the tailrace is interwoven with the large-scale backflow and inflow. Only a small amount of water flowed upward along the tailrace, and the backflow and flow near the wall formed an intense shear flow. This shear layer continuously curls and splits, significantly influenced by the "S" characteristics. When entering the reverse pump region deeply after passing through the braking zone, serious cavitation may occur in the tailrace. Influence of the cavitation phase change on the mass disturbance and wave speed variation, and the influence of the mass excitation source on the external and pressure pulsation characteristics of the unit. The mass excitation source intensified the fluctuation amplitude of the pressure in the tailrace and enlarged the cavitation region, generating an array of intricate flow features within the tailrace amid the load rejection progression.

4. CONCLUSION

This study utilized a multiphase flow model to conduct numerical simulations and analyses of the full-flow-domain load rejection process of water pumps and turbines, primarily aiming to investigate the mechanism behind the cavitation characteristics during the procedure of rejecting load. The subsequent deductions were formulated:

(1) The flow characteristics primarily exhibited dynamic instability. Throughout the load rejection process, there was a significant fluctuation in the pressure pulsation in the non-blade area, leading to a notable variation in the torque on the main shaft of the unit, posing the risk of fatigue deformation in the main shaft. The high-frequency pressure pulsations demonstrated increasing periodic fluctuations. As the movable guide vanes close and a speed-flow effect occurs, the disruption of the flow state in the non-blade area becomes more pronounced.

(2) Flow separation and vortex phenomena were clearly observable. The rapid decrease in flow results in widespread vortices, and the expansion and compression of vortices in the cavitation chamber cause a sudden drop in local pressure. The vortices in the inlet areas of the blades were extensive and persistent. Under reverse pump conditions, the internal flow of the impeller exhibits a distinct semi-cavitation state with flow separation and turbulent backflow in the flow passage. The vortices filled the blade channels, and the air pockets propagated towards the outlet.

(3) Cavitation development induces shaft eccentricity, shaft whirl, and shaft system wear and may even lead to rotor-stator collisions. The expulsion effect of the air pockets reduces the effective water passage area, influencing the incidence angle at the impeller inlet and resulting in non-closed radial trajectories. The intricate flow characteristics of the water pumps and turbines during the transition process are underscored by various influencing factors.

(4) The evolution of tailrace flow patterns is substantial. The emergence of helical cavitation vortices may trigger unit vibrations, and a substantial amount of backflow causes a sharp increase in the flow velocity at the pipe wall, leading to severe cavitation. The mass excitation source of the cavitation phase change intensifies pressure fluctuations, consequently expanding the cavitation area and significantly impacting the performance of water pumps and turbines.

ACKNOWLEDGEMENTS

The National Natural Science Foundation of China provided support for this research (Grant No. 52066011: A study on the optimization of active guide vanes of pump turbines and the effect of their control theory on internal flow characteristics).

CONFLICT OF INTEREST

The authors declare no conflicts of interest regarding the present work or results.

AUTHORS CONTRIBUTION.

Qifei Li: Conceptualization, Methodology, Software. **Lu Xin:** Data curation, Writing- Original draft preparation Software, Validation, Writing- Reviewing and Editing. **Lei Yao:** Visualization, Investigation. **Shiang Zhang:** Supervision.

DATA AVAILABILITY

The authors are willing to provide the data upon reasonable request.

REFERENCES

Chen, D., & Xie, H. (2001). Internal flow characteristics of low specific speed pump-turbine in "S" characteristic region. *Journal of Hydraulic*

Engineering, *2001*(2), 76-78+84. https://doi.org/10.3321/j.issn:0559-9350.2001.02.014

Fu, X., & Li, D. (2018). Dynamic instability of a pump-turbine in load rejection transient process. *Science China Technological Sciences*, *61*(11), 1765-1775. https://doi.org/10.1007/s11431-017-9209-9

Goyal, R., & Gandhi, B. K. (2018). Review of hydrodynamics instabilities in Francis turbine during off-design and transient operations. Renewable Energy, 116: 697-709https://doi.org/10.1016/j.renene.2017.10.012

Hasmatuchi, V., Farhat, M., & Roth S. (2011). Experimental evidence of rotating stall in a pump-turbine at off design conditions in generating mode. *Journal of Fluids Engineering*, *133*(5), 623-635. https://doi.org/10.1115/1.4004088

Kubota, T., & Kushimoto, S. (1978). Visual observation of internal flow through high-head pump-turbine. *Fuji Electric Review*, *26*(4), 133-144. https://doi.org/10.13245/j.hust.201118

Le, Z., Xiao, Y., & Gui, Z. (2018). Analysis of pressure pulsation and internal flow characteristics in pump-turbine at extremely low guide vane opening in reverse pump mode. *Journal of Hydraulic Engineering*, *49*(12), 1541-1549. https://doi.org/10.13243/j.cnki.slxb.20180794

Li, B. (2012). Characteristics study of pump-turbine in reverse pump mode. *Technology Wind*, *2012*, (14), 155. https://doi.org/10.19392/j.cnki.1671-7341.2012.14.127

Li, Q., Chen, X., & Cai, T. (2021). Study on influence of asynchronous guide vane on unit characteristics under different arrangement modes. *Acta Energiae Solaris Sinica*, *42*(8), 23-31. (In Chinese). https://doi.org/10.19912/j.0254-0096.tynxb.2019-0769

Li, Q., Zhang, Z., & Li, R. (2018). Pressure pulsation characteristics in the bladeless area of a pump-turbine with MGV device. *Journal of Drainage and Irrigation Machinery Engineering*, *2018*(12). https://doi.org/10.3969/j.issn.1674 -8530.16.0318

Li, W., Li, Z., & Han, W. (2023). Time-mean equation and multi-field coupling numerical method for low-Reynolds-number turbulent flow in ferrofluid. *Physics of Fluids*, *35*(12), 125145. https://doi.org/10.1063/5.0179961

Liu, J., Li, Z., & Wang, L. (2011). Numerical Simulation of the Transient Flow in a Radial Flow Pump during Stopping Period, *Journal of Fluids Engineering*, *133* (11). 111101-1-7. https://doi.org/10.1115/1.4005137

Luo, X. (2022). Study on the influence of "S" characteristics of pumped storage units on load rejection transition process [D, Huazhong University of Science and Technology]. https://doi.org/10.27157/d.cnki.ghzku.2022.004940

Mao, X., Chen, D., & Wang, Y. (2021). Investigation on optimization of self-adaptive closure law for load rejection to a reversible pump turbine based on CFD. *Journal of Cleaner Production*, *283* (0), 124739-124739. https://doi.org/10.1016/j.jclepro.2020.124739

Pejovic, S., Krsmanovic, L., & Jemcov, R. (1976). *Unstable operation of high-head reversible pump-turbines*. *IAHR's 8th Symposium, Leningrad, USSR*, 1976. https://doi.org/10.3969/j.issn.2096-093X.1976.05.039

Peng, Y., Liu, C., & Gao, Y. (2021). Influence of characteristic curve and runner selection on transition process of pumped storage power station, *Hydropower and Pumped Storage*, *7*(5), 70-75. (In Chinese). https://doi.org/10.3969/j.issn.2096-093X.2021.05.011

Qian, Z., Zheng, B., & Yang, J. (2008). Effects of different guide vanes on pressure pulsation in hydro turbines. *Journal of Wuhan University*, *41*(6), 51-54. https://doi.org/10.3969/j.issn.1021-8952.2008.06.037

Wan, Z. (2023). *Optimization of the closing law of francis turbine guide vanes and inverse prediction analysis of the transition process* [D , Nanchang University]. https://doi.org/10.27232/d.cnki.gnchu.2023.003849

Xiao, Y., & Xiao, R. (2014). Transient simulation of a pump-turbine with misaligned guide vanes during turbine model start-up. *Acta Mechanica Sinica*, *30*(5), 646-655. https://doi.org/10.1007/s10409-014-0061-6

Xu, L., Peng, Y., & Tang W. (2022). Pump turbine in zone state S characteristics and pressure fluctuation research. *Water dynamics research and progress in A series*, *2022* (02), 213-225. https://doi.org/10.16076/j.cnki.cjhd.2022.02.009

Zeng, W., Yang, J., & Hu, J. (2017) Pumped storage system model and experimental investigations on S-induced issues during transients. Mechanical Systems and Signal Processing, 90: 350-364. https://doi.org/10.1016/j.ymssp.2016.12.031

Zhai, L., Wang Z., & Li Z. (2016). TEHD analysis of a bidirectional thrust bearing in a pumped storage unit. *Industrial Lubrication and Tribology*, *68*(3). 315-324. https://doi.org/10.1108/ilt-07-2015-0092

Zhang, Y., Zheng, X., & Li, J. (2019) Experimental study on the vibrational performance and its physical origins of a prototype reversible pump turbine in the pumped hydro energy storage power station. *Renewable Energy*, *130*. pp. 667-676. https://doi.org/10.1016/j.renene.201

Zuo, Z., Fan, H., & Liu, S. (2015). S-shaped characteristics on the performance curves of pump-turbines in turbine mode - A review. *Renewable & Sustainable Energy Reviews. 60*(0), 836-851. https://doi.org/10.1016/j.rser. 2015.12.312.